Bio-Design and Manufacturing (2023) 6:507–521
https://doi.org/10.1007/s42242-023-00240-8

RESEARCH ARTICLE

Benidipine-loaded nanoflower-like magnesium silicate improves bone regeneration

Jingyi Lu[1,2] · Miao Sun[1,2] · Jingyu Zhang[1,2] · Xiaofu Yang[1,2] · Minyi Dong[1,5] · Huihui He[1,2] · An Liu[3,4] · Mengfei Yu[1,2] · Baixiang Wang[1,2] · Huiming Wang[1,2]

Received: 18 October 2022 / Accepted: 24 February 2023 / Published online: 16 June 2023

Abstract

Regeneration and reconstruction of bone tissue is always a challenge for clinicians due to the uncertainty of bone repair materials in terms of long-term and efficient effects on osteoblasts. Here, we propose a novel strategy combining benidipine, an antihypertensive drug and nanoparticles to synergistically promote the healing of bone defects. Loose and porous benidipine-loaded magnesium silicate nanoparticles were prepared and validated for their biosafety. The nanoparticles were efficiently taken up by preosteoblasts and uniformly distributed around the nucleus. After internalization into cells, the nanosystem is degraded by lysosomes, and the effect of promoting osteogenic differentiation is reflected by the continuous release of benidipine, silicon and magnesium ions. Our results clearly evaluated that the nanoflower-like magnesium silicate delivering benidipine tends to be more appropriate for the bone regeneration in preosteoblasts, indicating that it might be a potential approach in guiding bone repair in clinical applications.

Jingyi Lu, Miao Sun and Jingyu Zhang have contributed equally to this work.

✉ Mengfei Yu
yumengfei@zju.edu.cn

✉ Baixiang Wang
wangbaixiang@zju.edu.cn

✉ Huiming Wang
whmwhm@zju.edu.cn

[1] The Affiliated Hospital of Stomatology, School of Stomatology, Zhejiang University School of Medicine, Hangzhou 310000, China

[2] Key Laboratory of Oral Biomedical Research of Zhejiang Province, Hangzhou 310000, China

[3] Department of Orthopedics, The Second Affiliated Hospital, Zhejiang University School of Medicine, Hangzhou 310009, China

[4] Orthopedics Research Institute of Zhejiang University, Hangzhou 310009, China

[5] Zhangjiagang Hospital of Traditional Chinese Medicine, Suzhou 215600, China

Graphic abstract

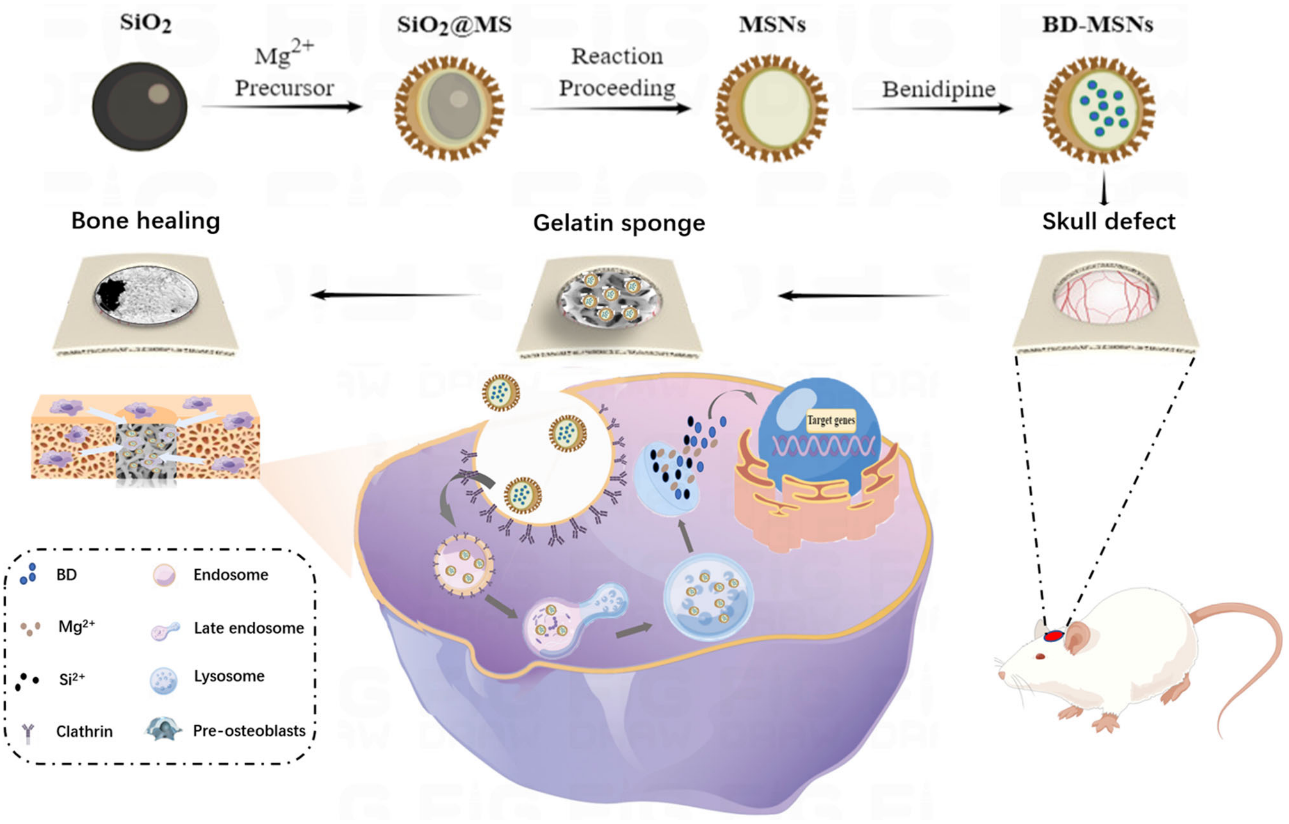

Keywords Nanoparticles · Benidipine · Bone tissue engineering · Endocytosis

Introduction

Hypertension is a major risk factor for untimely death worldwide, mainly as a result of cardiovascular complications [1]. According to statistics, more than 640 million people suffer from hypertension around the world, and the number is still increasing further [2]. In addition to cardiovascular complications, hypertension is associated with metabolic bone diseases characterized by the loss of bone density, such as osteorosis and osteoarthritis [3–5]. The relationship between hypertension and osteoporosis has now become the consensus on certain points. A prospective study is published confirming that the exacerbated calcium loss associated with hypertension may lead to an increased risk of hip fracture [6, 7]. It has been suggested that systemic vascular pathology also plays a key role in the etiology of osteoarthritis (OA) [8]. Hypertension biophysically and biochemically disrupts joint homeostasis, increases intraosseous pressure and induces hypoxia, which in turn impacts the remodeling of subchondral bone and the osteochondral junction. In addition to above-mentioned bone diseases, hypertension negatively affects alveolar bone quality, delaying bone healing in extraction sockets [9–11]. All above studies have shown that hypertension seems to be closely related to metabolic bone diseases, but the intrinsic mechanism remains unclear.

Hypertension is thought to alter calcium metabolism, leading to accelerated calcium depletion [12]. Some issues, such as increased sympathetic nervous system activity, enhanced inflammatory responses, and altered parathyroid hormone regulation, are all involved in this process [13, 14]. Responsively, antihypertensive drugs can affect bone metabolism in different ways: thiazide diuretics appear to prevent fractures by promoting calcium reabsorption at the distal convoluted tubule [15]. Angiotensin II receptor blockers (ARBs) avoid overactivation of sympathetic nerves by blocking the angiotensin II receptor, possibly reducing inflammatory cytokine production and promoting bone repair [16–18]. Among them, our previous study [19] found that benidipine, a drug for hypertension, can stimulate the osteogenic differentiation of preosteoblasts, and the bone morphogenetic protein-2 (*BMP2*)/recombinant mothers against decapentaplegic homolog 1 (*SMAD*) signaling pathway is the key pathway for this biological effect, which is consistent with Imai and Ma [20, 21]. All evidence supports the relative hypothesis between hypertension and metabolic bone disease.

Another delicate task is that bone repair in hypertensive patients takes a longer period. Conventional bone regeneration involves a series of biological events including early inflammation, matrix deposition and mineralization and bone remodeling [22]. Insufficient blood circulation caused by cardiovascular disease adversely affects bone metabolism and osteogenesis. In addition, high sodium intake, a major cause of hypertension, may increase urinary calcium loss and affect mineral deposition in bone defect areas, thereby prolonging bone healing progression. Repository preparation is more conducive to repairing bone defects, and engineered nanomicrospheres with sustained-release function may be a potential therapy. In particular, hollow magnesium silicate nanoparticles (MSNs) have emerged as an effective vehicle to transfer cargo for local delivery, slow release, and reduce side effects [23]. MSNs are not only bone graft substitutes but also biomaterials that can effectively promote osteogenic differentiation [24].

Above all, we prepared nanoflower-like benidipine-loaded magnesium silicate nanoparticles (BD-MSNs) using a chemical templating method and investigated the internalization mechanism in mouse embryo osteoblast precursor cells (MC3T3-E1). BD-MSNs can be efficiently taken up by preosteoblasts and promote osteogenic differentiation under their interaction. The in vivo calvarial defect model verified that BD-MSNs can effectively repair bone defects under the dual functions of directly promoting osteogenic differentiation and indirectly regulating the osteogenic environment by lowering blood pressure. The results confirm that the local application of BD-MSNs provides a possibility for the repair of bone defects in hypertensive patients.

Materials and methods

Materials

Benidipine (BD), ammonium hydroxide solution, and (3-aminopropyl)triethoxysilane (APTES) were obtained from Aladdin (China). Tetraethyl orthosilicate (TEO), fluorescein isothiocyanate isomer I (FITC), and Lyso-Tracker Red were purchased from Solarbio (China). Ethanol, magnesium chloride hexahydrate ($MgCl_2{\cdot}6H_2O$), and ammonium chloride were acquired from Macklin (China). The cell counting kit-8 (CCK-8) was purchased from Dojindo Molecular Technologies (Japan). Fetal bovine serum (FBS), a-minimum essential medium (a-MEM), trypsin (0.25%), 4,6-diamidino-2-phenylindole (DAPI), and phalloidin-TRITC (tetraethyl rhodamine isothiocyanate) were obtained from Gibco (USA). The BCIP/NBT alkaline phosphatase color development kit, alkaline phosphatase assay kit, and penicillin were purchased from Beyotime (China).

Synthesis of nanoparticles

Silica colloidal spheres were first prepared by the classical Stöber method according to a previous report [25]. Ammonia (2 mol/L) and deionized water (10 mol/L) were stirred in a beaker containing 70 mL of ethanol for 25 min, and then 0.4 mol TEO solution was added dropwise to the above solution and stirred slowly. The solution in the container gradually became milky white after 30 min, and stirring was continued for 4 h until a stable colloidal suspension was formed. The suspension was centrifuged at 8000 r/min for 10 min, washed three times with water and ethanol, and then centrifuged and dried to obtain the final silica colloid spheres. To obtain MSNs, we weighed 200 mg of silica colloidal spheres and placed them in an aqueous solution containing 1.5 mmol $MgCl_2{\cdot}6H_2O$, 20 mmol ammonium chloride and 2 mL ammonia. After the colloidal balls were evenly dispersed in the mixed solution, they were placed into the reactor for a 160 °C hydrothermal reaction, and the whole process lasted for 12 h. The modified MSN-based samples were further dried using a vacuum dryer for the preparation of powder samples. For the synthesis of BD-MSNs, 6 mg BD was completely dissolved in 1 mL dimethyl sulfoxide (DMSO), and then 10 mg MSNs were added and vigorously shaken in an ultrasonic cleaner for 10 min. Hydrochloric acid (1%) was added under stirring to dilute the above solution to a volume of 20 mL. After stirring at 600 r/min for 24 h, the BD-MSNs were collected by centrifugation, washed three times with water to remove unloaded drugs, and dried at 60 °C. To verify the successful payload of the drug, the concentration of the drug that was washed off in the supernatant was detected by high-performance liquid chromatography (Agilent 1290, Agilent, USA), and finally, the drug loading rate of the sample was calculated by the following formula:

$$\begin{aligned}\text{Drug loading rate} = {} & (\text{the total mass of benidipine} \\ & - \text{the mass of benidipine in the supernatant})/ \\ & \text{the total mass of nanoparticles} \times 100\%.\end{aligned}$$

Characterization of MSNs and BD-MSNs

The morphology of the synthesized MSNs was observed using scanning electron microscopy (SEM, Gemini SEM 300, Carl Zeiss AG, Germany) and transmission electron microscopy (TEM, JEM-1400flash, JEM, Japan). The MSN-based sample solutions were dropped onto carbon tapes or copper mesh and dried naturally at room temperature. The phase structure was determined by X-ray diffraction (XRD, Bruker D8 ADVACNCE, Bruker, Germany) with a scan (2θ) range from 5° to 90°. Fourier transform infrared spectroscopic (FTIR, Nicolet 670, Thermo Fisher, USA) analysis was used to characterize the chemical composition of the samples. The elemental composition mappings of Si and Mg were measured by energy dispersive spectrometer (EDS) analysis (GeminiSEM 300, Carl Zeiss AG, Germany). The particle size distribution and zeta potential of MSNs and BD-MSNs were tested by a laser particle size and zeta potential analyzer (Zetasizer Nano-ZS, Malvern, UK). The thermal stability of BD-MSNs was checked by a thermal gravimetric analyzer (TGA, Mettler Toledo, Switzerland) with a thermal range from 0 to 800 °C. To verify the slow-release properties of the nanoparticles, 10 mg BD-MSNs were dissolved in phosphate buffer saline (PBS, pH 7.4) and uniformly oscillated in a 200 r/min constant temperature shaker and the supernatant at different time points was collected. The concentration of benidipine released from the sample was analyzed by high-performance liquid chromatography. The concentration of silicon and magnesium ions released from the sample was analyzed by inductively coupled plasma-mass spectrometry (ICP-MS, NexION 300XX, PerkinElmer, USA).

Cell culture and viability detection

The preosteoblast cell line MC3T3-E1 was purchased from ATCC (American type culture collection). Cells were cultured in a-MEM (Cienry, China) containing 10% FBS and 100 U/mL penicillin in humidified air with 5% CO_2 at 37 °C. The medium was changed every three days. Trypsin (25%) was used for cell passaging and digestion. To evaluate the viability of MC3T3-E1 cells, cells were evenly spread on the bottom of a 96-well plate at a density of 8000 cells per well. MSNs or BD-MSNs medium dilutions were added at a concentration of 12.5, 25, 50, 100, and 200 μg/mL and coincubated for 24 h at 37 °C and 5% CO_2. The CCK-8 kit was used to test their cytocompatibility, and the tested optical density (OD) value at 450 nm was recorded and repeated three times using a microplate reader (Infinite F50, TECAN, Hombrechtikon, Switzerland).

Blood compatibility test

Briefly, BD-MSNs were added to PBS/red blood cell (RBC) suspensions at concentrations of 12.5, 25, 50, 100, and 200 μg/mL. The same number of RBCs incubated with 0.5 mL PBS or water was used as a negative or positive control, respectively. The samples were incubated on a shaker for 24 h and then centrifuged at 4000 r/min for 5 min. Broken RBCs release hemoglobin into the supernatant. A microplate reader was used to detect the OD value of the supernatant at 450 nm [26]. The percent hemolysis was calculated as follows: hemolysis = (sample absorbance−negative control)/(positive control−negative control)×100%.

Cellular uptake kinetics

Flow cytometry was used to analyze the cellular uptake kinetics of MSNs and BD-MSNs [27]. To label the MSN or BD-MSN surface with fluorescence, 4 mg of FITC, 400 mg of sodium hydroxide and 500 μL of APTES were first dissolved in 5 mL of absolute ethanol and protected from light at room temperature for 24 h to form a homogeneous liquid. Fifty milligrams MSNs or BD-MSNs were added to the FITC mixture, ethanol was added to bring the solution volume to 20 mL, and the mixture was protected from light for 12 h, washed three times with 95% ethanol, and then vacuum-dried at 60 °C to obtain FITC-MSNs or FITC-BD-MSNs [28]. MC3T3-E1 cells were seeded at 1×10^5 cells/well in 6-well plates for 24 h and then incubated with 50 μg/mL FITC-MSNs or FITC-BD-MSNs for different times (1, 4, 8, 12, 24, 48 h) for the time-dependent uptake assay. Cellular uptake was evaluated by flow cytometry (CytoFLEX S, Beckman, USA).

Cellular uptake pathways

MC3T3-E1 cells were seeded at 1×10^5 cells/well in 6-well plates for 24 h. To analyze the endocytosis mechanism, inhibitors of various uptake pathways were applied. Cells were first pretreated with chlorpromazine (CHL, 10 μg/mL), amiloride (AMI, 50 mmol/L), nocodazole (NOC, 10 μg/mL), or nystatin (NYS, 10 μg/mL) for 30 min, and then MSNs or BD-MSNs were added for coculture for 4 h. Flow cytometry was used to obtain data showing endocytosis efficiency and statistical analysis was performed. For the energy-dependent intake assay, cells were precooled at 4 °C before adding MSNs or BD-MSNs. The medium was replaced with serum-free medium (SFM) to analyze the effect of serum on cellular uptake.

Fluorescence images of BD-MSNs in MC3T3-E1 cells

For the in vitro imaging, 50 μg/mL BD-MSNs were cocultured with MC3T3-E1 cells in 6-well plates for 4 h. After washing twice with PBS, the cells were fixed with 4% paraformaldehyde at 37 °C for 15 min. Phalloidin solution (1:250) was added to each well for 30 min. After washing three times with 0.05% Tween/PBS, DAPI staining solution was added dropwise to soak the cells, and the cells were incubated in the dark for 10 min and washed with PBS again. The samples were observed by a laser scanning confocal microscopy (LSCM, Leica, dmi8, Germany). To explore the positional relationship between nanoparticles and lysosomes in cells, MC3T3-E1 cells were incubated with BD-MSNs for 4 h as described above. A small amount of LysoTracker Red was added to the medium at a ratio of 1:13,333, mixed well, preheated at 37 °C, replaced with the original medium and incubated for 30 min. Cells were washed twice with PBS, fixed and counterstained with DAPI. The samples were observed by LSCM.

Intracellular distribution of BD-MSNs by TEM

MC3T3-E1 cells were passaged at a ratio of 1:3 and seeded in T25 sterile culture flasks. When the cells reached 80% confluence, 50 μg/mL BD-MSNs were added and incubated for 1, 4, 8, 12, 24, and 48 h. After washing with PBS and trypsinizing, cell pellets were harvested and fixed overnight at 4 °C in 2.5% glutaraldehyde. The next day, the samples were rinsed three times with 0.1 mol/L phosphate buffer at pH 7.0 and fixed with 1% osmic acid solution for 1.5 h. The samples were subsequently dehydrated with graded ethanol solutions and embedded with Spurr embedding medium. The slices were prepared at 70 nm in an ultramicrotome (LEICA, UC7, Germany) and observed in a Hitachi H-7650 TEM (Japan).

Osteogenic effects in vitro

After the cells were seeded in a 6-well plate at a density of 1×10^5 cells/well and adhered to the wall, the growth medium was replaced with an osteoinductive medium treated with different components and cultured continuously. The medium was changed every two days. Cells were harvested on Days 3 and 7, and total RNA was extracted using the TRIzol method [29]. The total RNA of each sample was taken for reverse transcription, and the gene expression of alkaline phosphatase (*ALP*), collagen-1 (*COL-1*), osteocalcin (*OCN*), and runt-related transcription factor 2 (*RUNX2*) was determined by RT-qPCRs (real-time quantitative PCR).

Alkaline phosphatase staining

MC3T3-E1 cells were treated differently in 6-well plates and cultured in osteogenic induction medium for 7 days. Alkaline phosphatase staining was performed according to the instructions of the alkaline phosphatase quantitative and qualitative kit. The stained cells were observed and imaged with an inverted microscope (Olympus CKX41, Japan).

Alizarin red staining

MC3T3-E1 cells were treated differently in 6-well plates and cultured in osteogenic induction medium for 21 days. Cells were fixed with ice ethanol for 1 h, washed twice with PBS, added to 1% alizarin red staining solution at 37 °C for 30 min, and washed gently with deionized water. The formation of calcium nodules in each group was observed and photographed under an inverted optical microscope. Subsequently, the dye was eluted by 10% cetylpyridine chloride for 1 h. The collected dye solution was transferred to a 96-well plate, and the absorbance value was obtained at a wavelength of 540 nm using a microplate reader.

In vivo biosafety

In vivo biosafety was first examined before the use of BD-MSNs for the treatment of calvarial defects in rats. We injected nanoparticles of different components into the tail vein of rats, sacrificed the rats four weeks after injection, and removed the heart, liver, spleen, lung, and kidney for hematoxylin–eosin (HE) staining.

In vivo imaging observation

To study the local metabolism of nanoparticles in vivo, indocyanine green (ICG)-labeled BD-MSNs were prepared by the above method and placed in the skull defect of mice in strict accordance with the surgical procedures, and in vivo imaging was performed on Days 0, 1, 3, and 7 to observe the local fluorescence retention.

Bone regeneration in vivo

To evaluate the effect of bone regeneration in vivo, we established a rat skull defect model. All experimental protocols and animal handling procedures were approved by the Institutional Animal Care and Use Committee (IACUC), with the ethical number ZJCLA-IACUC-20020031. A total of 40 rats weighing 200–300 g were randomly divided into four groups, namely blank control, BD, MSNs and BD-MSNs. To make the biologics work better locally, gelatin sponge was used as a carrier to carry the BD solution or nanoparticle suspension into the defects. The whole animal experimental procedure was as follows: rats were anesthetized, and a longitudinal incision with a length of approximately 2 cm was prepared for the calvarial bone defect model. The skin and deep fascia were incised layer by layer to expose the bone surface. Use a hollow trephine bur to drill a hole with a diameter of 5 mm on the left and right sides of the cranial suture, and do not penetrate the meninges. Differently treated sterile gelatin sponges were then placed over the bone defect. Soft tissue was closed with a 4–0 suture. After the operation, 10 U/kg penicillin was injected intramuscularly for three days to prevent infection. Four and eight weeks after surgery, the calvarial bone was removed, fixed in 4% paraformaldehyde solution for 48 h, and then analyzed by micro-computed tomography (micro-CT). Analysis was performed at 80 kV and 80 mA using a micro-CT system (MILabs, U-CT-XUHR, Netherlands) to quantify the mineralized tissue ingrowth inside the defect. After micro-CT imaging, the samples were immersed in ethylene diamine tetraacetic acid (EDTA) decalcification solution for one month. The samples were then dehydrated in a series of ethanol solutions and embedded in paraffin, and 5 μm sections were prepared for hematoxylin and eosin (H&E) staining and immunohistochemical staining of RUNX2 and CD31.

Statistical analysis

All numerical data are expressed as the mean±standard deviation (SD). Statistical analysis was performed by independent sample's *t* test. One-way analysis of variance (ANOVA) was used to compare multiple groups and $p<0.05$ was considered to be statistically significant. All statistical analyses were performed using SPSS 22.0 software (SPSS, Chicago, IL, USA).

Results and discussion

BD-MSNs with good physicochemical properties were prepared

In this work, nanosilicon dioxide was used as the template, and magnesium chloride was used as the magnesium source to wrap the template by the chemical deposition method as mentioned in previous study [30]. After purification, the morphology and structure of MSNs and BD-MSNs were further observed. SEM showed that the prepared silica colloidal spheres were round, smooth, and uniform, showing ideal stability (Fig. 1a). After grafting on magnesium by the chemical sacrificial method, MSNs showed a shape similar to bayberry, with a loose and porous surface (Fig. 1b). The hydrothermal reaction did not affect the homogeneity of the nanoparticles, whose particle size was similar to that of silica colloidal spheres. More interestingly, through the cross-section of the nanoparticle, we found that its interior is a hollow structure, and the flower-like edge exposes the pores through the inside and outside. The results of TEM also confirmed its loose and porous structure (Figs. 1c and 1d). The EDS results described the spatial distribution of silicon and magnesium ions, confirming the successful incorporation of magnesium into the MSNs (Figs. 1e–1h).

XRD patterns of SiO_2, MSNs and BD-MSNs were recorded and are displayed in Fig. 1i. SiO_2 exhibited only one broad peak at 22° due to its composition of amorphous silica, of which the reactivity is greatly enhanced [31]. Peaks at 20°, 32.5°, 34.9°, 52.8°, 60.5°, and 71.6° were found in the MSNs, which corresponded to magnesium silicate crystals ($Mg_3Si_4O_9(OH)_4$) according to JCPDS (Joint Committee on Powder Diffraction Standards) No. 03–0174 [32]. The addition of benidipine did not change the position of the characteristic peaks of MSNs. To further confirm the formation of MSNs, FTIR was used to analyze the chemical structures of the samples (Fig. 1j). In the spectrum of SiO_2, the bands at 798, 1219, and 1042 cm^{-1} were attributed to the stretching and deformation vibrations of SiO_2. The bands at 1633 and 3421 cm^{-1} were ascribed to O–H vibrations from adsorbed water [33]. No other bands were observed, suggesting that pure SiO_2 fibers were prepared successfully. After the hydrothermal reaction, MSNs and BD-MSNs showed characteristic absorption peaks at approximately 667, 793, 1015, 1628, and 3443 cm^{-1}. The weak absorption peak at 667 cm^{-1} corresponds to the stretching vibration of Si–O–Mg. The weak absorption peaks at 793 and 1015 cm^{-1} correspond to the bending vibration and stretching vibration of Si–O–Si, respectively [34]. The peak at 1015 cm^{-1} corresponds to the new bonds formed outside Si–O–Si. The absorption peak at 1628 cm^{-1} corresponds to the stretching vibration of hydrogen-bonded water molecules. The broad absorption peak appearing near 3443 cm^{-1} was associated with the characteristic absorption bands for Mg–OH [35]. These results demonstrate the transformation process from SiO_2 to MSNs during the hydrothermal reaction. In addition, compared with the infrared spectrum results of Benidipine in Fig. S1 (Supplementary Information), BD-MSNs showed the characteristic peaks consistent with the pure Benidipine at 2968 and 3265 cm^{-1}, representing N–H and CH_3, respectively; that is, benidipine was successfully loaded into BD-MSNs. The specific surface area and pore size distribution were investigated by nitrogen (N_2) adsorption–desorption measurements, as shown in Fig. 1k. The isotherms of flower-like MSNs showed typical type IV curves with H4 hysteresis loops. The calculated Brunauer–Emmett–Teller (BET) surface area was 235.37 m^2/g, and the mean diameter and pore volume were 3.74 nm and 0.20 cm^3/g (Fig. 1l), respectively, revealing that MSNs have a good loading capacity for biologic agents. As displayed in Fig. 1m, MSNs are negatively charged in aqueous solution. BD-MSNs have a slightly higher zeta potential than MSNs. The results of thermogravimetric analysis showed that only 10% of the mass of MSNs was lost when the temperature was increased to 181 °C, which may be explained by the volatilization of benidipine. When it reaches a high temperature of 800 °C, the mass drops to 72.57%, which proves that the material has thermal stability (Fig. 1n). The supernatant was detected to calculate the drug loading rate of the nanoparticles. As shown in Fig. S2 (Supplementary Information), the standard curve of benedipine is plotted. According to the formula calculated in the above method, MSNs can effectively encapsulate a large amount of benidipine with a drug loading rate of 334.52 mg/g, owing to the high specific surface area of MSNs. The release kinetics of the drug showed that BD release could be slowly sustained, and the cumulative release of BD from BD-MSNs

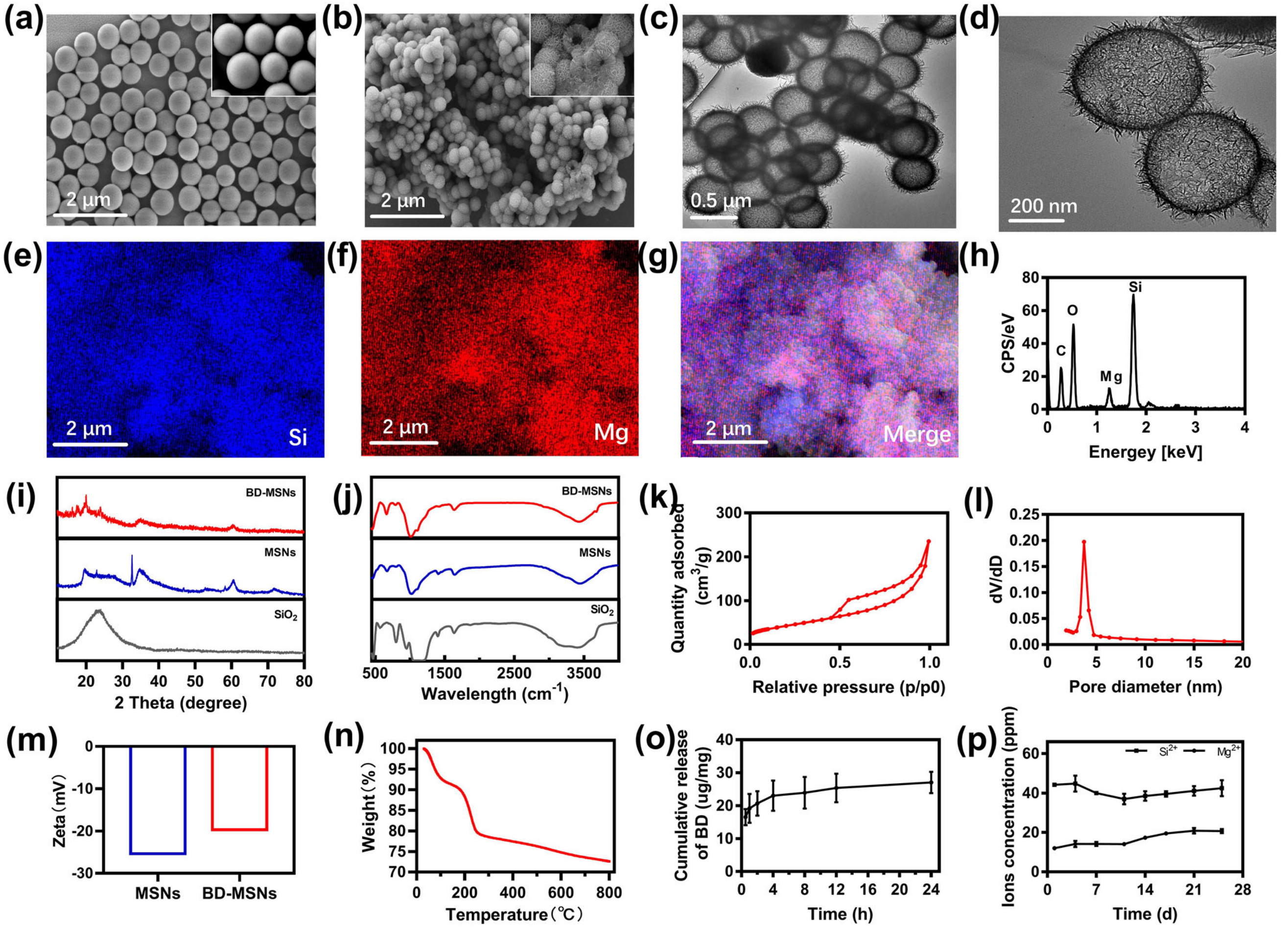

Fig. 1 Magnesium silicate nanoparticles (MSNs) with good physicochemical properties were prepared. **a**, **b** Representative scanning electron microscopy (SEM) images of SiO_2 nanoparticles and MSNs. The magnifications are 10000× and 60000×. **c** A transmission electron microscopy (TEM) image of MSNs. **d** Magnified image of picture (**c**). **e**–**g** Elemental mapping (Si, Mg, Merge) of MSNs. **h** Results of compositional analysis of MSNs using energy dispersive spectrometer (EDS). **i** X-ray diffraction (XRD) patterns of SiO_2 (gray), MSNs (blue), and benidipine-loaded magnesium silicate nanoparticles (BD-MSNs) (red). **j** Fourier transform infrared spectroscopic (FTIR) spectra of SiO_2 (gray), MSNs (blue), and BD-MSNs (red). **k** N_2 adsorption–desorption isotherms of MSNs. **l** Pore diameter distribution of MSNs. **m** Zeta analysis of MSNs and BD-MSNs. **n** Thermogravimetric curves of MSNs. **o** Cumulative release of Benidipine HCl (BD) over 24 h (*n*=3). **p** Cumulative release of silicon and magnesium ions over 25 d (*n*=3)

within 24 h was 27.014 μg/mg (Fig. 1o). As shown in Fig. 1p, silicon and magnesium ions can also be slowly released with the degradation of MSNs. As two basic elements in bone minerals, the release of silicon and magnesium provides certain biological activity for materials in the bone reconstruction field [36].

BD-MSNs have better biocompatibility and can be efficiently taken up by preosteoblasts

To explore the biological activity of BD-MSNs in vitro, we detected the effect of different samples on cell proliferation. In this study, MC3T3-E1 subclone 24 was selected as the experimental cell line because it has multiple subclones and can be used as a good model for studying osteoblast differentiation in vitro. The CCK8 results showed that MSNs and BD-MSNs have good cytocompatibility in the concentration range of 12.5–200 μg/mL (Fig. 2a). According to our previous studies, the optimal concentration of BD was 0.005–0.542 μg/mL [19]. Considering the drug loading and slow-release characteristics of MSNs, we finally selected 12.5 μg/mL MSNs and BD-MSNs and 0.338 μg/mL BD as the subsequent experimental concentrations. The BD-MSNs also had excellent blood compatibility, as evidenced by the low hemolytic index even at a high concentration of 200 μg/mL (Fig. 2b). Collectively, these results provide favorable evidence for the excellent biocompatibility of BD-MSNs for the delivery of therapeutics.

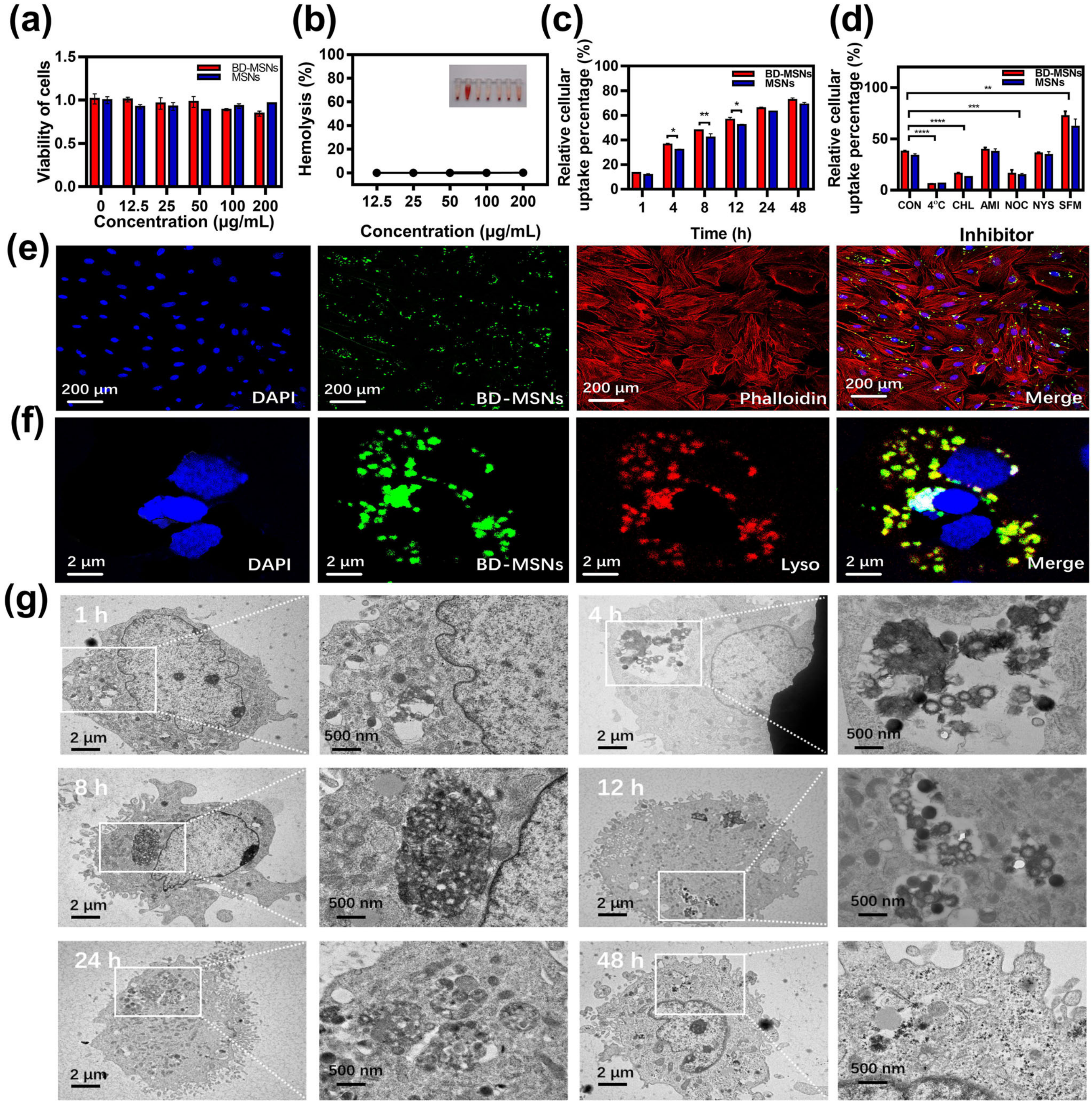

Fig. 2 Benidipine-loaded magnesium silicate nanoparticles (BD-MSNs) have better biocompatibility and can be efficiently taken up by preosteoblasts. **a** Cell viability of MC3T3-E1 incubated with magnesium silicate nanoparticles (MSNs) and BD-MSNs at concentrations ranging from 0–200 μg/mL for 24 h (n=3; *p< 0.05, ***p<0.001). **b** A hemolysis test was conducted to evaluate the blood compatibility of BD-MSNs at various concentrations (n=3). **c** Cellular uptake effects of MSNs and BD-MSNs for 1–48 h (n=3; *p<0.05, **p<0.01). **d** Quantitative analysis of the influencing factors of uptake using different treatments, including chlorpromazine, amiloride, nystatin, low-temperature (4 °C), and serum-free treatment (n=3; *p<0.05, **p<0.01, ***p<0.001). **e** Laser scanning confocal microscopy (LSCM) images of MC3T3-E1 cells treated with the BD-MSNs (green), 4,6-diamidino-2-phenylindole (DAPI, blue), and phalloidin (red). **f** LSCM images of the intracellular distribution of fluorescein isothiocyanate isomer I (FITC)-modified BD-MSNs in MC3T3-E1 cells, followed by treatment with LysoTracker Red. **g** Transmission electron microscopy (TEM) images of MC3T3-E1 cells treated with BD-MSNs for 1 h to 48 h

The cellular uptake of MSNs is the first and most important step in exerting biological effects. First, we explored the internalization efficiency of MSNs and BD-MSNs. As shown in Fig. 2c, the nanoparticles could be efficiently taken up by MC3T3-E1 cells, in a time-dependent manner. The internalization rate of MSNs has exceeded 30% within 4 h. This may be attributed to its soft surface structure. Compared with smooth and hard solid spherical structures, hollow structures with flocculent surfaces are more likely to adhere to cells and be further taken up because they provide more cell binding sites and are prone to compression and deformation when interacting with cells [37–39]. Notably, the internalization efficiency of BD-MSNs was found to be significantly higher than that of MSNs at 4, 8, and 12 h. The interaction process between particles and cells strongly depends on the physicochemical properties of the particles themselves, such as surface chemistry [40], size [41], morphology [42], surface potential [43], and functionalization [44, 45]. The positive charge on the nanoparticle surface is easier to combine with the negative charge on the cell membrane surface [46]. The higher surface charge of BD-MSNs than MSNs may explain its improved uptake efficiency. Moreover, BD is a lipid-soluble compound, that is more likely to interact with the cell membrane and directly penetrate into the cell interior [47].

The internalization of nanoparticles occurs via clathrin-dependent endocytosis

Endocytosis is a critical step in the process by which many therapeutic nanodrugs reach their intracellular target sites. To reveal the internalization mechanism of MSNs and BD-MSNs, we applied CHL (10 μg/mL), AMI (50 μg/mL), and NYS (10 μg/mL) as relative endocytosis inhibitors. CHL is a phenothiazine-derived antipsychotic drug (APD) that may inhibit clathrin-mediated endocytosis (CME) in cells by inhibiting AP2 [48]. AMI inhibits the exchange of sodium ion channels and sodium hydrogen ions and is an inhibitor of the macropinocytosis pathway [49]. NYS binds to cholesterol and affects cell membrane fluidity, which in turn mediates pathways including lipid rafts, cholesterol-enriched microdomains, and caveolae [50]. Flow cytometry analysis showed that the uptake of MSNs and BD-MSNs by CHL-treated cells was significantly reduced, while the application of the other two inhibitors did not affect the internalization of the samples, demonstrating that the internalization of nanoparticles occurs via clathrin-dependent endocytosis rather than caveolae-dependent endocytosis or macropinocytosis (Fig. 2d). Such endocytosis may involve a complex process, including (1) cytoplasmic proteins involved in endocytosis forming a coated pit; (2) plasma membrane bending and invagination; (3) intracellular vesicles formed after separation of invaginated necks; (4) release and recovery of substances in vesicles [51].

Nocodazole (NOC) inhibits the dynamics of microtubules and promotes their depolymerization, thereby affecting cellular endocytosis [52]. The uptake of MSNs and SD-MSNs was also significantly reduced in cells pretreated with nocodazole, suggesting that microtubules are involved in the internalization of MSNs and BD-MSNs. Low-temperature (4 °C) treatment reduces membrane fluidity and significantly inhibits cellular uptake [53]. Our data show that there are still a few nanoparticles that can be taken up by cells with 4 °C of preconditioning, demonstrating that energy-independent internalization is also involved. Apart from that, in the absence of serum (SFM), MSNs and BD-MSNs bind more tightly to the cell membrane, and the endocytosis efficiency is higher, which indicates that serum protein binding on the nanoparticle surface partly hinders the interaction between MSNs and cells.

BD-MSNs are uniformly distributed in the cytoplasm and mostly colocalize with lysosomes

To better distinguish the localization of nanoparticles, the fluorescence of BD-MSNs in MC3T3-E1 cells was observed using LSCM. We observed FITC-labeled nanoparticles in the cytoplasm surrounding the nucleus (Fig. 2e). After uptake by cells, nanomaterials are mainly located in the lysosome (Fig. 2f). Nanoparticles are endocytosed into cells and enter early endosomes, which can be recycled to the cell surface or enter late endosomes and then integrated into lysosomes [54]. Lysosomes are associated with autophagy and affect cell activity, apoptosis, and function. Yang et al. [55] found that autophagy is activated after nanoparticles are taken into cells, promoting osteogenesis and promoting autophagosome formation by binding to LC3 and p62.

To better visualize the internalization of nanoparticles, we collected cells at different time points, processed, embedded, and sliced them for TEM observation. TEM showed that the MSNs were successfully internalized into cells, usually in clusters (Fig. 2g). After internalization, the number of lysosomes around the nanoparticles increased. To a large extent, our results demonstrate that MSNs can maintain long-term stability in vitro to warrant their function as nanocarriers for drug delivery. Nanoparticles typically have three fates after being ingested by cells: The first is degradation by lysosome enzymes, which are most suitable for degradable particles [56]. In addition, some nanoparticles may be partially degraded and reduced in size and then eliminated by exocytosis [57]. Furthermore, most inorganic colloidal nanoparticles and nanoparticles made from nondegradable polymers cannot be degraded or easily excreted because they are exceptionally stable and relatively large in size [58]. With the extension of the culture time, the nanoparticles were continuously digested by the cells. After MSNs were incubated with MC3T3-E1 for 48 h, a large number of nanoparticles lost their original morphology.

BD-MSNs promote osteogenic differentiation and mineralization of preosteoblasts

To investigate the role of BD-MSNs in promoting osteogenesis in vitro, MC3T3-E1 cells were cocultured with different samples (BD, MSNs and BD-MSNs) for 3 and 7 days. After 3 days, the expression of *OCN* in each group was significantly upregulated, and the level of *OCN* expression in the BD-MSN group was the most significant. On Day 7, the gene expression of *ALP*, *COL*-1, *OCN* and *RUNX2* in the BD, MSN and BD-MSN groups was higher than that in the control group, and the difference was statistically significant (p<0.05) (Figs. 3a and 3b). As shown in Fig. 3c, the ALP staining results showed that MC3T3-E1 cells treated in the BD, MSN, and BD-MSN groups exhibited significantly higher *ALP* activity, with the most evident staining in the BD-MSN group. Similar results were obtained with Alizarin red staining on Day 21 (Fig. 3d).

Osteoblasts are thought to be able to sense and respond to silicon. Silica transporters are present in plants, bacteria and lower eukaryotes, and recent studies have shown that they are also present in mammals [59–61]. During the cross-linking of proteoglycans and collagen, silicon not only stabilizes the bone matrix but also inhibits their degradation in vivo [62]. Silicate-based biomaterials have been reported to enhance bone formation [63, 64]. Interestingly, the incorporation of Mg^{2+} activates the canonical Wnt signaling pathway by inducing protein reactions and downstream gene expression. Activation of the pathway represses the tendency of mesenchymal stem cells to differentiate into the chondrogenic and adipogenic lineages while enhancing the tendency to differentiate into osteoblastic lineage [65]. Therefore, MSNs can promote the expression of seed cell-related osteogenic genes, mainly due to the release of silicon and magnesium.

Our previous study [19] found that BD, a kind of dihydropyridine-type calcium channel blocker (CCB), might suppress the possible function of osteoclasts through the *OPG/RANKL/RANK* signaling pathway and promote the differentiation of preosteoblasts toward osteogenic direction through the *BMP2/SMAD* signaling pathway. CCB tends to increase the alkaline phosphatase activity of osteoblasts and stimulate mineral matrix deposition [66]. On the other hand, osteoclasts can regulate the homeostasis of bone formation and bone remodeling to maintain bone homeostasis. Calcium signaling is a crucial aspect of osteoclast differentiation and function. *RANKL* activated Ca^{2+} signaling receptors in osteoclasts through intracellular Ca^{2+}

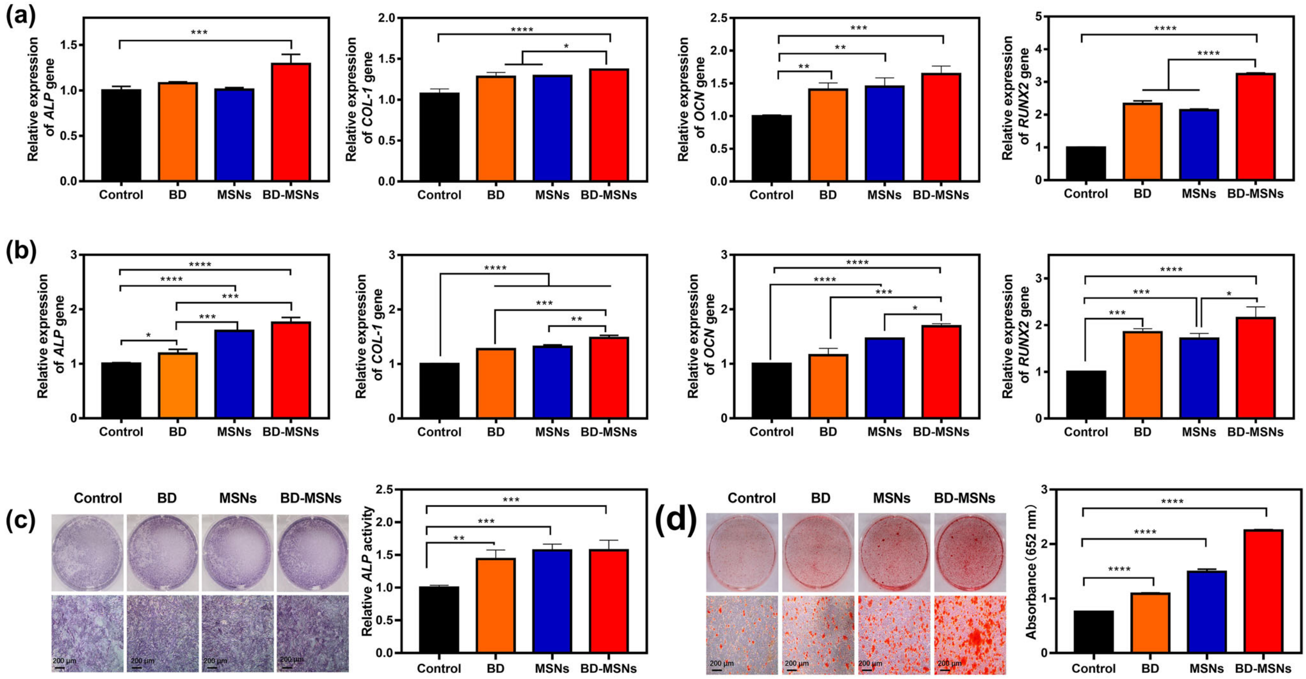

Fig. 3 Benidipine-loaded magnesium silicate nanoparticles (BD-MSNs) promote osteogenic differentiation and mineralization of preosteoblasts. **a** *ALP*, *COL-1*, *OCN*, and *RUNX2* gene expression on Day 3. **b** *ALP, COL-1, OCN* and *RUNX2* gene expression on Day 7. **c** *ALP* staining and quantitative analysis on Day 14. **d** Alizarin red staining on Day 21 and relative quantitative data through calcium nodule elution by 10% cetylpyridinium chloride (n=3; *p<0.05, **p<0.01, ***p<0.001)

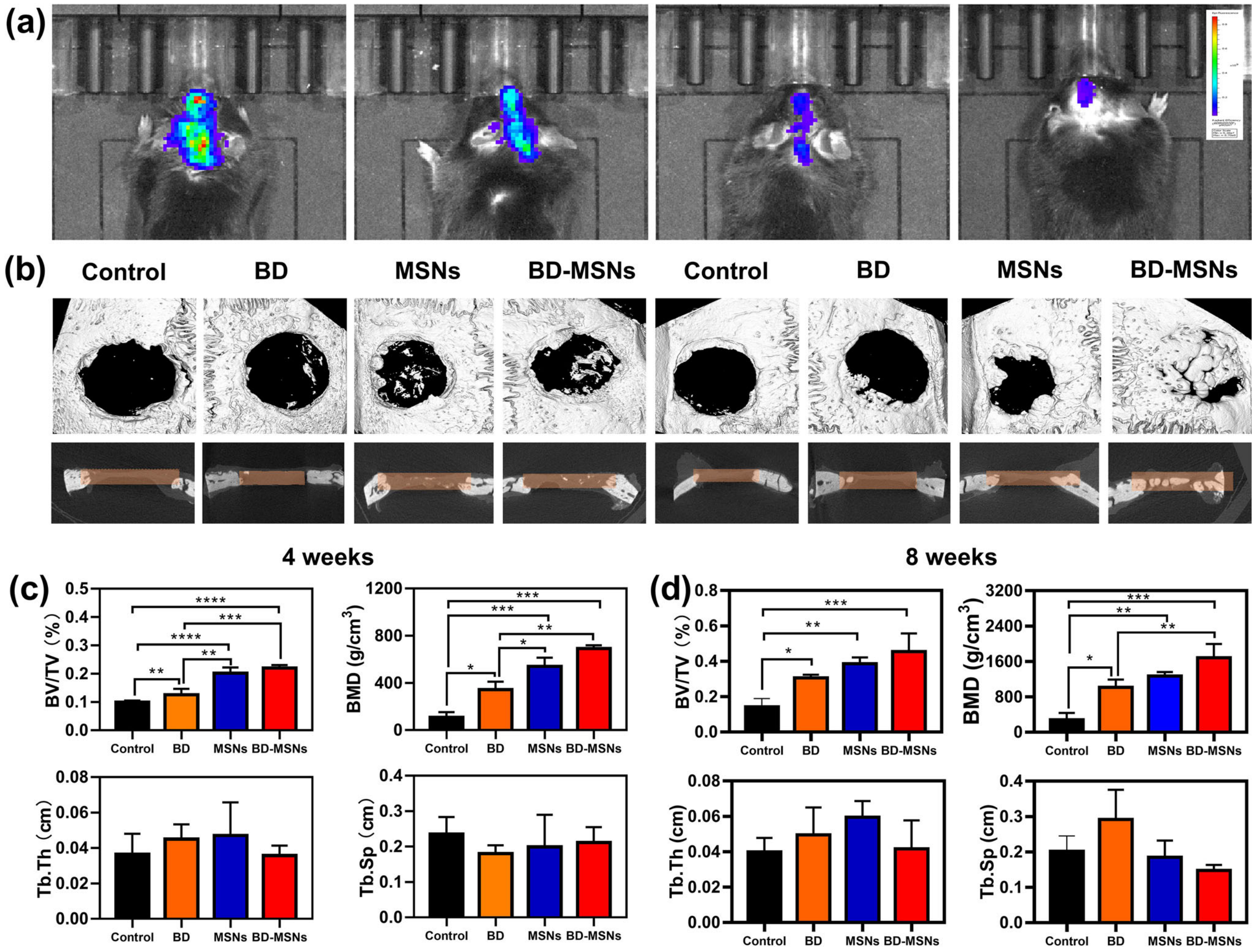

Fig. 4 Benidipine-loaded magnesium silicate nanoparticles (BD-MSNs) can promote bone healing in critical calvarial defects in rats. **a** Fluorescence imaging of the nude mouse treated with indocyanine green (ICG)-modified BD-MSNs in vivo. **b** 3D images from a reconstructed cranium by micro-computed tomography (micro-CT) and section view at weeks 4 and 8. The transverse section of the image shows gross osteogenesis, with the brown portion representing the prepared bone defect area. **c** The corresponding quantitative analysis (trabecular bone volume fraction (BV/TV), bone mineral density (BMD), trabecular thickness (Tb. Th), and trabecular separation (Tb. Sp)) of different groups after implantation in calvarial defects for four weeks (n=3; *p<0.05, **p<0.01, ***p<0.001). **d** The corresponding quantitative analysis (BV/TV, BMD, Tb. Th, Tb. Sp) of different groups after implantation in calvarial defects for eight weeks (n=3; *p<0.05, **p<0.01, ***p<0.001)

calmodulin (CaM). Binding of Ca^{2+} to CaM stimulates Ca^{2+}/CaM-dependent kinase (CaMK) and calcineurin, leading to activation of the osteoclast-related gene *NFATc1* [67]. Several calcium channel blockers did inhibit osteoclast differentiation and bone resorption by modulating calcium signaling. Additionally, benidipine is prone to indirectly regulate the reconstruction of bone defects by reducing blood pressure. Gratifyingly, BD-MSNs superimposed the biological effects of BD and MSNs and synergistically further promoted the osteogenic differentiation of MC3T3-E1 cells.

BD-MSNs can promote bone healing in critical calvarial defects in rats

We evaluated the in vivo biosafety of the nanoparticles. As shown in Fig. S3 (Supplementary Information), there was no visible damage to the naked eye after tail vein injection of the nanoparticle suspension in each experimental group of heart, liver, spleen, lung and kidney tissues. In the skull defect model, a gelatin sponge was used as a scaffold for each component implanted in the defect area. We performed in vivo imaging experiments in mice treated with gelatin sponges and BD-MSNs, and observed them for 7 days (Fig. 4a). The results showed that the gelatin sponge can effectively carry

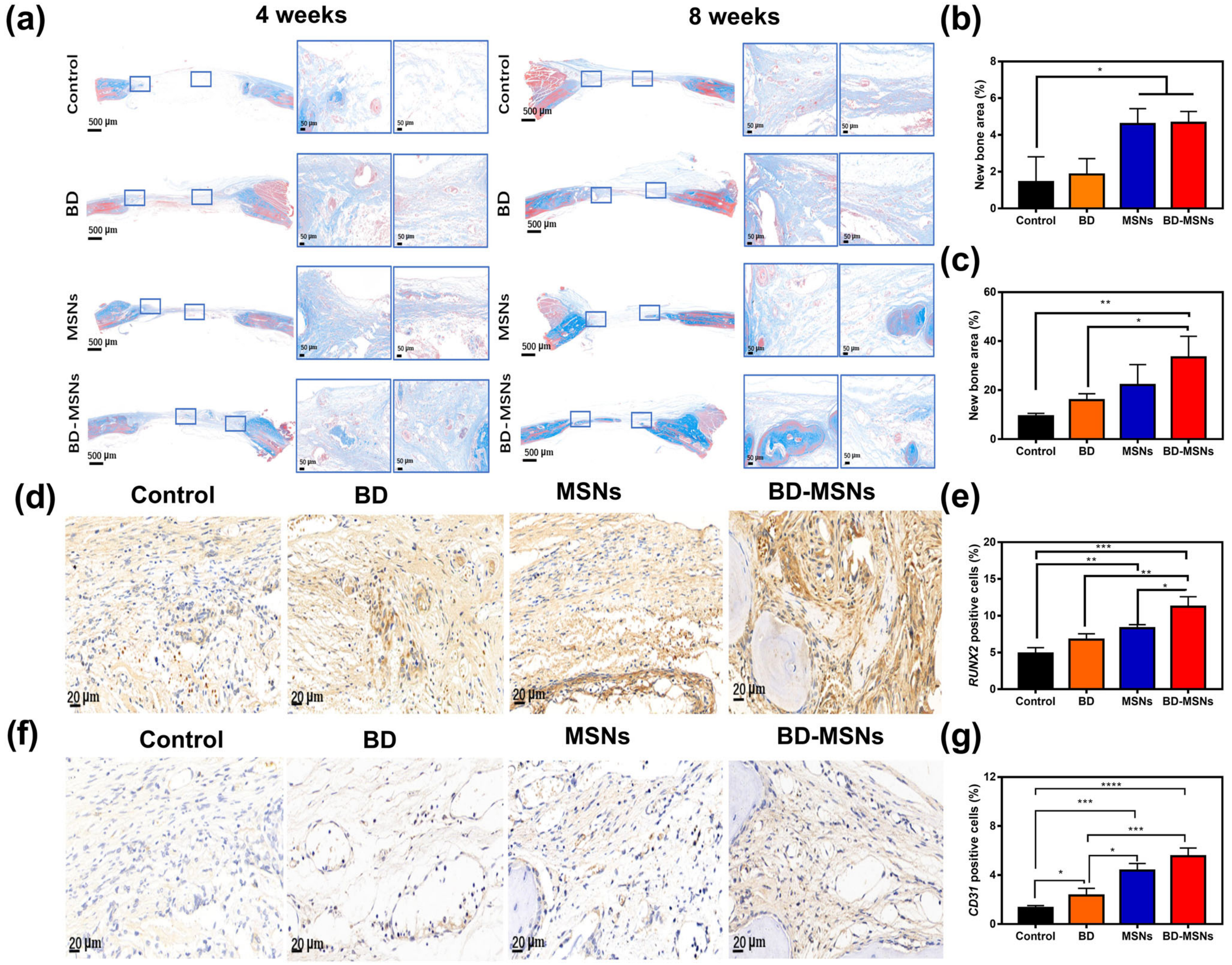

Fig. 5 More mineralized collagen fibers and higher expression of *RUNX2* and *CD31* were observed at the defect sites of the group of benidipine-loaded magnesium silicate nanoparticles (BD-MSNs). **a** Masson's trichrome staining images of the bone tissues at weeks 4 and 8. The left side is a general view of the section; the right side is the magnification of the center and marginal area of the tissues (blue box in the first column). **b** Statistical analysis of new bone area in the 4th week (n=3; *p<0.05, **p<0.01, ***p<0.001). **c** Statistical analysis of new bone area in the 8th week (n=3; *p<0.05, **p<0.01, ***p<0.001). **d** Representative *RUNX2* staining images in four treatment groups in the 8th week. **e** The corresponding quantitative data of the RUNX2-positive cells in the bone tissues in the four treatment groups in the 8th week (n=3; *p<0.05, **p<0.01, ***p<0.001). **f** Representative CD31 staining images in four treatment groups in the 8th week. **g** The corresponding quantitative data of the CD31-positive cells in the bone tissues in the four treatment groups in the 8th week (n=3; *p<0.05, **p<0.01, ***p<0.001)

the nanoparticles so that they can be localized in the skull defect, and a small amount of fluorescent signal can still be observed in the skull on Day 7, providing evidence that nanoparticles can favor local bone healing.

Benefiting from the long-acting and sustained-release effect of BD-MSN nanoparticles, potential bone repair in the critical skull defect areas will persist. The micro-CT images showed rare new bone formation in the control group after four weeks, while more new bone was formed in the BD-MSN group. In the 8th week, the bone healing in each group was much better, and the new bone formed in the BD-MSN group covered almost 85% of the bone defect area (Fig. 4b). Quantitative micro-CT analysis showed that the trabecular bone volume fraction (BV/TV) and bone mineral density (BMD) were significantly increased in the BD-MSN group compared with the other groups at weeks 4 and 8 (Figs. 4c and 4d).

H&E staining showed that throughout the bone repair process, a large amount of connective tissue and vascular tissue was distributed in the bone defect area. The bone defect area in the control group was mainly covered by fibrous connective tissue, while the BD, MSN and BD-MSN groups showed more mature bone tissue with more blood vessels and collagen production, which was consistent with the micro-CT results. After eight weeks, these flail-like tissues covered almost the entire bone defect in the BD-MSN group (Fig. S4 in Supplementary Information). The magnification views of MSNs and BD-MSNs show increased blood vessels. In addition, both BD and MSNs had been filled with fibrous tissue, while a larger blue area was displayed in the BD-MSN group (Fig. 5a). Some cuboid osteoblasts could be observed at the edge of the defects which indicated the formation of active osteogenesis. Statistical analysis of the newly formed bone area demonstrated that the BD-MSN group had the largest new bone area in the stage of the bone healing process (Figs. 5b and 5c). Furthermore, immunohistochemical staining of *RUNX2* and *CD31* was used to further determine the healing of rat calvaria under different treatments. Angiogenesis and bone defect reconstruction are complementary. *RUNX2* and *CD31* were highly expressed in the BD-MSN group, followed by the MSN group and the BD group, with the control group exhibiting the lowest expression (Figs. 5d–5g and Fig. S5 in Supplementary Information).

Conclusions

Hypertension affects bone metabolism and interferes with the normal healing of bone defects. Among many antihypertensive drugs, benidipine can not only relieve hypertension and thus indirectly regulate bone metabolism but also directly act on local bone tissue, which plays a dual role in promoting the repair of bone defects. The magnesium silicate nanoparticles we designed, as an ideal drug carrier, realize the long-acting and slow release of benidipine. Through the effect of synergistic promotion, this drug delivery system offers potential for future bone repair in hypertension.

Supplementary Information The online version contains supplementary material available at https://doi.org/10.1007/s42242-023-00240-8.

Acknowledgements This work was financially supported by the National Natural Science Foundation of China (Nos. 8212200044, 82071085, 31872752, and 81600909), the Zhejiang Provincial Natural Science Foundation of China (Nos. LR21H140001, LY22H140002, and LQ22C100003), the National Key Research and Development Program of China (No. 2018YFA0703000), and the Medical Technology and Education of Zhejiang Province of China (No. 2018KY501).

Author contributions JYL was involved in investigation, methodology, writing—original draft, formal analysis, and data curation; MS contributed to methodology, resources, and formal analysis; JYZ was involved in conceptualization, writing—original draft, and data curation; XFY and MYD contributed to methodology, project administration, supervision, and data curation; HHH and AL were involved in methodology, project administration, and resources; MFY contributed to methodology, project administration, resources, writing, review and editing, supervision, and data curation; BXW contributed to conceptualization, supervision, funding acquisition, and project administration; HMW was involved in conceptualization and resources.

Declarations

Conflict of interest MFY is an Associate Editor of *Bio-Design and Manufacturing*. The authors declare that they have no competing financial interests or personal relationships that could have appeared to influence the work reported in this paper.

Ethical approval All animal experimental protocols and handling procedures were approved by the Institutional Animal Care and Use Committee (IACUC), with the ethical number ZJCLA-IACUC-20020031.

References

1. Tibazarwa KB, Damasceno AA (2014) Hypertension in developing countries. Can J Cardiol 30(5):527–533. https://doi.org/10.1016/j.cjca.2014.02.020
2. Das P, Samarasekera U (2012) The story of GBD 2010: a "superhuman" effort. Lancet 380(9859):2067–2070. https://doi.org/10.1016/s0140-6736(12)62174-6
3. Javed F, Khan SA, Ayers EW et al (2012) Association of hypertension and bone mineral density in an elderly African American female population. J Natl Med Assoc 104(3–4):172–178. https://doi.org/10.1016/s0027-9684(15)30140-1
4. Manrique N, Pereira CC, Garcia LM et al (2012) Alveolar bone healing process in spontaneously hypertensive rats (SHR). A radiographic densitometry study. J Appl Oral Sci 20(2):222–227. https://doi.org/10.1590/s1678-77572012000200017
5. Yamamoto S, Kido R, Onishi Y et al (2015) Use of renin-angiotensin system inhibitors is associated with reduction of fracture risk in hemodialysis patients. PLoS ONE 10(4):e0122691. https://doi.org/10.1371/journal.pone.0122691
6. Cappuccio FP, Meilahn E, Zmuda JM et al (1999) High blood pressure and bone-mineral loss in elderly white women: a prospective study. Lancet 354(9183):971–975. https://doi.org/10.1016/s0140-6736(99)01437-3
7. Yang S, Nguyen ND, Center JR et al (2014) Association between hypertension and fragility fracture: a longitudinal study. Osteoporos Int 25(1):97–103. https://doi.org/10.1007/s00198-013-2457-8
8. Ching K, Houard X, Berenbaum F et al (2021) Hypertension meets osteoarthritis—revisiting the vascular aetiology hypothesis. Nat Rev Rheumatol 17(9):533–549. https://doi.org/10.1038/s41584-021-00650-x
9. Manrique N, Pereira CC, Luvizuto ER et al (2015) Hypertension modifies OPG, RANK, and RANKL expression during the dental socket bone healing process in spontaneously hypertensive rats. Clin Oral Investig 19(6):1319–1327. https://doi.org/10.1007/s00784-014-1369-0
10. Gealh WC, Pereira CC, Luvizuto ER et al (2014) Healing process of autogenous bone graft in spontaneously hypertensive rats treated with losartan: an immunohistochemical and histomorphometric study. J Oral Maxillofac Surg 72(12):2569–2581. https://doi.org/10.1016/j.joms.2014.07.010
11. Wu X, Al-Abedalla K, Eimar H et al (2016) Antihypertensive medications and the survival rate of osseointegrated dental implants: a cohort study. Clin Implant Dent Relat Res 18(6):1171–1182. https://doi.org/10.1111/cid.12414
12. Barzilay JI, Davis BR, Pressel SL et al (2017) The impact of antihypertensive medications on bone mineral density and fracture

risk. Curr Cardiol Rep 19(9):76. https://doi.org/10.1007/s11886-017-0888-0
13. Singh MV, Chapleau MW, Harwani SC et al (2014) The immune system and hypertension. Immunol Res 59(1–3):243–253. https://doi.org/10.1007/s12026-014-8548-6
14. Elefteriou F (2018) Impact of the autonomic nervous system on the skeleton. Physiol Rev 98(3):1083–1112. https://doi.org/10.1152/physrev.00014.2017
15. Kruse C, Eiken P, Vestergaard P (2016) Optimal age of commencing and discontinuing thiazide therapy to protect against fractures. Osteoporos Int 27(5):1875–1885. https://doi.org/10.1007/s00198-015-3451-0
16. Saravi B, Vollmer A, Lang G et al (2021) Impact of renin-angiotensin system inhibitors and beta-blockers on dental implant stability. Int J Implant Dent 7(1):31. https://doi.org/10.1186/s40729-021-00309-y
17. Mulinari-Santos G, de Souza Batista FR, Kirchweger F et al (2018) Losartan reverses impaired osseointegration in spontaneously hypertensive rats. Clin Oral Implants Res 29(11):1126–1134. https://doi.org/10.1111/clr.13376
18. Kwok T, Leung J, Barrett-Connor E et al (2017) ARB users exhibit a lower fracture incidence than ACE inhibitor users among older hypertensive men. Age Ageing 46(1):57–64. https://doi.org/10.1093/ageing/afw150
19. Wang B, Yang J, Fan L et al (2021) Osteogenic effects of antihypertensive drug benidipine on mouse MC3T3-E1 cells in vitro. J Zhejiang Univ-Sci B (Biomed & Biotechnol) 22(5):410–420. https://doi.org/10.1631/jzus.B2000628
20. Imai M, Ayukawa Y, Yasunami N et al (2019) Effect of a single injection of benidipine-impregnated biodegradable microcarriers on bone and gingival healing at the tooth extraction socket. Adv Wound Care 8(3):108–117. https://doi.org/10.1089/wound.2018.0834
21. Ma ZP, Liao JC, Zhao C et al (2015) Effects of the 1, 4-dihydropyridine L-type calcium channel blocker benidipine on bone marrow stromal cells. Cell Tissue Res 361(2):467–476. https://doi.org/10.1007/s00441-015-2115-x
22. Lopes D, Martins-Cruz C, Oliveira MB et al (2018) Bone physiology as inspiration for tissue regenerative therapies. Biomaterials 185:240–275. https://doi.org/10.1016/j.biomaterials.2018.09.028
23. Sun TW, Zhu YJ, Qi C et al (2016) Templated solvothermal synthesis of magnesium silicate hollow nanospheres with ultrahigh specific surface area and their application in high-performance protein adsorption and drug delivery. J Mater Chem B 4(19):3257–3268. https://doi.org/10.1039/c5tb02632f
24. Bohner M (2009) Silicon-substituted calcium phosphates—a critical view. Biomaterials 30(32):6403–6406. https://doi.org/10.1016/j.biomaterials.2009.08.007
25. Stöber W, Fink A, Bohn E (1968) Controlled growth of monodisperse silica spheres in the micron size range. J Colloid Interface Sci 26(1):62–69. https://doi.org/10.1016/0021-9797(68)90272-5
26. Dou G, Tian R, Liu X et al (2020) Chimeric apoptotic bodies functionalized with natural membrane and modular delivery system for inflammation modulation. Sci Adv 6(30):eaba2987. https://doi.org/10.1126/sciadv.aba2987
27. Penaloza JP, Marquez-Miranda V, Cabana-Brunod M et al (2017) Intracellular trafficking and cellular uptake mechanism of PHBV nanoparticles for targeted delivery in epithelial cell lines. J Nanobiotechnol 15:1. https://doi.org/10.1186/s12951-016-0241-6
28. Xu X, Zhang K, Zhao L et al (2014) Characteristics of three sizes of silica nanoparticles in the osteoblastic cell line, MC3T3-E1. RSC Adv 4:46481. https://doi.org/10.1039/C4RA06863G
29. Ban E, Kwon H, Seo H et al (2021) Screening of miRNAs in plasma as a diagnostic biomarker for cardiac disease based on optimization of extraction and qRT-PCR condition assay through amplification efficiency. BMC Biotechnol 21:50. https://doi.org/10.1186/s12896-021-00710-w
30. Wang B, Meng W, Bi M et al (2013) Uniform magnesium silicate hollow spheres as high drug-loading nanocarriers for cancer therapy with low systemic toxicity. Dalton Trans 42(24):8918–8925. https://doi.org/10.1039/c3dt50659b
31. Zhao C, Yang J, Jiang B (2017) Rational design of hierarchical macroporous–mesoporous magnesium silicate for highly efficient removal of organic dye and Pb^{2+}. RSC Adv 7:47225. https://doi.org/10.1039/C7RA08766G
32. Cao L, Weng W, Chen X et al (2017) Promotion of in vivo degradability, vascularization and osteogenesis of calcium sulfate-based bone cements containing nanoporous lithium doping magnesium silicate. Int J Nanomed 12:1341–1352. https://doi.org/10.2147/IJN.S124965
33. Shen T, Gao M, Zang W et al (2018) Architecting organo silica nanosheets for regenerable cost-effective organics adsorbents. Chem Eng J 331:211–220. https://doi.org/10.1016/j.cej.2017.08.084
34. Gui CX, Wang QQ, Hao SM et al (2014) Sandwichlike magnesium silicate/reduced graphene oxide nanocomposite for enhanced Pb^{2+} and methylene blue adsorption. ACS Appl Mater Interfaces 6(16):14653–14659. https://doi.org/10.1021/am503997e
35. Bawaked S, Narasimharao K (2020) Structural and catalytic properties of copper silicate nanomaterials. Sci Rep 10:518. https://doi.org/10.1038/s41598-020-57502-z
36. Niu Y, Guo L, Hu F et al (2020) Macro-microporous surface with sulfonic acid groups and micro-nano structures of PEEK/nano magnesium silicate composite exhibiting antibacterial activity and inducing cell responses. Int J Nanomed 15:2403–2417. https://doi.org/10.2147/IJN.S238287
37. Teng Z, Wang C, Tang Y et al (2018) Deformable hollow periodic mesoporous organosilica nanocapsules for significantly improved cellular uptake. J Am Chem Soc 140(4):1385–1393. https://doi.org/10.1021/jacs.7b10694
38. Sun H, Wong EHH, Yan Y et al (2015) The role of capsule stiffness on cellular processing. Chem Sci 6(6):3505–3514. https://doi.org/10.1039/c5sc00416k
39. Key J, Palange AL, Gentile F et al (2015) Soft discoidal polymeric nanoconstructs resist macrophage uptake and enhance vascular targeting in tumors. ACS Nano 9(12):11628–11641. https://doi.org/10.1021/acsnano.5b04866
40. Du XJ, Wang JL, Iqbal S et al (2018) The effect of surface charge on oral absorption of polymeric nanoparticles. Biomater Sci 6(3):642–650. https://doi.org/10.1039/c7bm01096f
41. Ma N, Ma C, Li C et al (2013) Influence of nanoparticle shape, size, and surface functionalization on cellular uptake. J Nanosci Nanotechnol 13(10):6485–6498. https://doi.org/10.1166/jnn.2013.7525
42. Zhang D, Wei L, Zhong M et al (2018) The morphology and surface charge-dependent cellular uptake efficiency of upconversion nanostructures revealed by single-particle optical microscopy. Chem Sci 9(23):5260–5269. https://doi.org/10.1039/c8sc01828f
43. Bewersdorff T, Gruber A, Eravci M et al (2019) Amphiphilic nanogels: influence of surface hydrophobicity on protein corona, biocompatibility and cellular uptake. Int J Nanomed 14:7861–7878. https://doi.org/10.2147/IJN.S215935
44. Zhao Z, Ukidve A, Krishnan V et al (2019) Effect of physicochemical and surface properties on in vivo fate of drug nanocarriers. Adv Drug Deliv Rev 143:3–21. https://doi.org/10.1016/j.addr.2019.01.002
45. Bertoli F, Garry D, Monopoli MP et al (2016) The intracellular destiny of the protein corona: a study on its cellular internalization and evolution. ACS Nano 10(11):10471–10479. https://doi.org/10.1021/acsnano.6b06411

46. Zhao F, Zhao Y, Liu Y et al (2011) Cellular uptake, intracellular trafficking, and cytotoxicity of nanomaterials. Small 7(10):1322–1337. https://doi.org/10.1002/smll.201100001
47. Rodriguez PL, Harada T, Christian DA et al (2013) Minimal "self" peptides that inhibit phagocytic clearance and enhance delivery of nanoparticles. Science 339(6122):971–975. https://doi.org/10.1126/science.1229568
48. Daniel JA, Chau N, Abdel-Hamid MK et al (2015) Phenothiazine-derived antipsychotic drugs inhibit dynamin and clathrin-mediated endocytosis. Traffic 16(6):635–654. https://doi.org/10.1111/tra.12272
49. Henriksen L, Grandal MV, Knudsen SL et al (2013) Internalization mechanisms of the epidermal growth factor receptor after activation with different ligands. PLoS ONE 8(3):e58148. https://doi.org/10.1371/journal.pone.0058148
50. Hao M, Mukherjee S, Sun Y et al (2004) Effects of cholesterol depletion and increased lipid unsaturation on the properties of endocytic membranes. J Biol Chem 279(14):14171–14178. https://doi.org/10.1074/jbc.M309793200
51. Munoz A, Costa M (2012) Elucidating the mechanisms of nickel compound uptake: a review of particulate and nano-nickel endocytosis and toxicity. Toxicol Appl Pharmacol 260(1):1–16. https://doi.org/10.1016/j.taap.2011.12.014
52. Rejman J, Oberle V, Zuhorn IS et al (2004) Size-dependent internalization of particles via the pathways of clathrin- and caveolae-mediated endocytosis. Biochem J 377(Pt 1):159–169. https://doi.org/10.1042/BJ20031253
53. Wei X, Liu N, Song J et al (2022) Effect of silica nanoparticles on cell membrane fluidity: the role of temperature and membrane composition. Sci Total Environ 838:156552. https://doi.org/10.1016/j.scitotenv.2022.156552
54. Zhao H, Lin ZY, Yildirimer L et al (2016) Polymer-based nanoparticles for protein delivery: design, strategies and applications. J Mater Chem B 4(23):4060–4071. https://doi.org/10.1039/c6tb00308g
55. Yang G, Liu H, Hu X et al (2017) Bio-inspired hybrid nanoparticles promote vascularized bone regeneration in a morphology-dependent manner. Nanoscale 9(18):5794–5805. https://doi.org/10.1039/c7nr00347a
56. Vtyurina N, Aberg C, Salvati A (2021) Imaging of nanoparticle uptake and kinetics of intracellular trafficking in individual cells. Nanoscale 13(23):10436–10446. https://doi.org/10.1039/d1nr00901j
57. Donahue ND, Acar H, Wilhelm S (2019) Concepts of nanoparticle cellular uptake, intracellular trafficking, and kinetics in nanomedicine. Adv Drug Deliv Rev 143:68–96. https://doi.org/10.1016/j.addr.2019.04.008
58. Ali MS, Uttinger MJ, Romeis S et al (2022) Effect of protein adsorption on the dissolution kinetics of silica nanoparticles. Colloids Surf B Biointerfaces 214:112466. https://doi.org/10.1016/j.colsurfb.2022.112466
59. Ma JF, Yamaji N (2015) A cooperative system of silicon transport in plants. Trends Plant Sci 20(7):435–442. https://doi.org/10.1016/j.tplants.2015.04.007
60. Garneau AP, Carpentier GA, Marcoux AA et al (2015) Aquaporins mediate silicon transport in humans. PLoS ONE 10(8):e0136149. https://doi.org/10.1371/journal.pone.0136149
61. Ha SW, Viggeswarapu M, Habib MM et al (2018) Bioactive effects of silica nanoparticles on bone cells are size, surface, and composition dependent. Acta Biomater 82:184–196. https://doi.org/10.1016/j.actbio.2018.10.018
62. Hung CC, Chaya A, Liu K et al (2019) The role of magnesium ions in bone regeneration involves the canonical Wnt signaling pathway. Acta Biomater 98:246–255. https://doi.org/10.1016/j.actbio.2019.06.001
63. Takaoka S, Yamaguchi T, Tanaka K et al (2013) Fracture risk is increased by the complication of hypertension and treatment with calcium channel blockers in postmenopausal women with type 2 diabetes. J Bone Miner Metab 31(1):102–107. https://doi.org/10.1007/s00774-012-0389-6
64. Macon ALB, Li S, Chung JJ et al (2016) Ductile silica/methacrylate hybrids for bone regeneration. J Mater Chem B 4(36):6032–6042. https://doi.org/10.1039/c6tb00968a
65. Lin K, Liu Y, Huang H et al (2015) Degradation and silicon excretion of the calcium silicate bioactive ceramics during bone regeneration using rabbit femur defect model. J Mater Sci Mater Med 26(6):197. https://doi.org/10.1007/s10856-015-5523-2
66. Kim HJ, Lee J, Lee GR et al (2021) Flunarizine inhibits osteoclastogenesis by regulating calcium signaling and promotes osteogenesis. J Cell Physiol 236(12):8239–8252. https://doi.org/10.1002/jcp.30496
67. Kang JY, Kang N, Yang YM et al (2020) The role of Ca^{2+}-NFATc1 signaling and its modulation on osteoclastogenesis. Int J Mol Sci 21(10):3646. https://doi.org/10.3390/ijms21103646